

## Research Article

# The Pore Structure of Marine to Continental Transitional Shales in the Permian Shanxi Formation on the East Margin of the Ordos Basin, China

Tao Wang,<sup>1,2</sup> Fenghua Tian,<sup>3</sup> Ze Deng<sup>1</sup>,, Haiyan Hu<sup>1</sup>,,<sup>4</sup> and Zhitao Xie<sup>1</sup>

<sup>1</sup>School of Geosciences, Yangtze University, Wuhan, Hubei 430100, China

<sup>2</sup>PetroChina Research Institute of Petroleum Exploration & Development, Beijing 100083, China

<sup>3</sup>Exploration and Development Division of PetroChina Coalbed Methane Company Limited, Beijing 100083, China

<sup>4</sup>School of Resource and Environment, Yangtze University, Wuhan, Hubei 430100, China

Correspondence should be addressed to Ze Deng; [dengze@petrochina.com.cn](mailto:dengze@petrochina.com.cn) and Haiyan Hu; [1064069334@qq.com](mailto:1064069334@qq.com)

Received 5 May 2022; Revised 19 June 2022; Accepted 20 July 2022; Published 22 August 2022

Academic Editor: Dengke Liu

Copyright © 2022 Tao Wang et al. This is an open access article distributed under the Creative Commons Attribution License, which permits unrestricted use, distribution, and reproduction in any medium, provided the original work is properly cited.

The pore structure is an important factor in determining the storage capacity for shale gas development. Twelve samples were selected from the marine to continental transitional shales in the Shanxi Formations on the eastern margin of the Ordos Basin, and their nanoscale pore structure was investigated by a variety of low-temperature N<sub>2</sub> adsorption (LT-N<sub>2</sub>GA) and low-pressure CO<sub>2</sub> adsorption (LP-CO<sub>2</sub>GA) and high-pressure mercury intrusion (HPMI) experiments. The shale pores are complex and are mainly mesopores, which range mainly from 10 nm to 40 nm and greatly contribute to the pore volume (PV), whereas pores with a diameter less than 0.8 nm greatly contribute to the specific surface area (SSA) of the shale. The pore structure is affected by the TOC content, organic matter maturity, and illite/smectite (I/S) mixed layer content. The total PV increases with the increase in TOC content, organic matter maturity, and I/S mixed layer content. The effects of pores on the occurrence shale gas were determined by high-pressure methane adsorption experiments. The maximum adsorption amount of methane was positively correlated with the SSA of the micropores, indicating that the micropores have a large SSA, which controlled the adsorbed gas content of the shale. The mesopores provide the majority of the PV, which mainly corresponds to the volume of free gas in the shale, and the macropores are mainly micron-sized pores, which can form the main migration channels for shale gas.

## 1. Introduction

China's shale gas exploration and production have made considerable strides in marine shales, notably in the southern Sichuan Basin, after the success of shale gas in North America [1–4]. In 2020, China reported a total production of  $200 \times 10^8 \text{ m}^3$  of shale gas. Marine to continental transitional shales have attracted scant attention than marine shales, which is mostly found in delta facies where rapid sedimentary environment changes have caused the transitional shale to be thinner and less continuous, making it difficult for development [5, 6]. Nonetheless, the transitional shale gas resources are large, approximately  $19.8 \times 10^{12} \text{ m}^3$  or 25% of China's shale gas reserve [7–9]. Future research on

the exploration and development of shale gas in China will focus on the transition shales [8].

Shale reservoirs are nano- to micrometer-scale complex and heterogeneous porous solid media having low porosity and poor permeability [10, 11]. Shale gas normally exists in three states: free, adsorbed, and dissolved. The adsorption state of shale gas occurs mostly on the surfaces of organic compounds and inorganic minerals, while the free-state state occurs predominantly in pores and microcracks and the dissolved state occurs predominantly in liquid hydrocarbons and water [12]. The IUPAC classification of pores is divided into three main categories: micropores (<2 nm), mesopores (2–50 nm), and macropores (>50 nm) [13]. The pores in shale are further categorized into three types based on their form

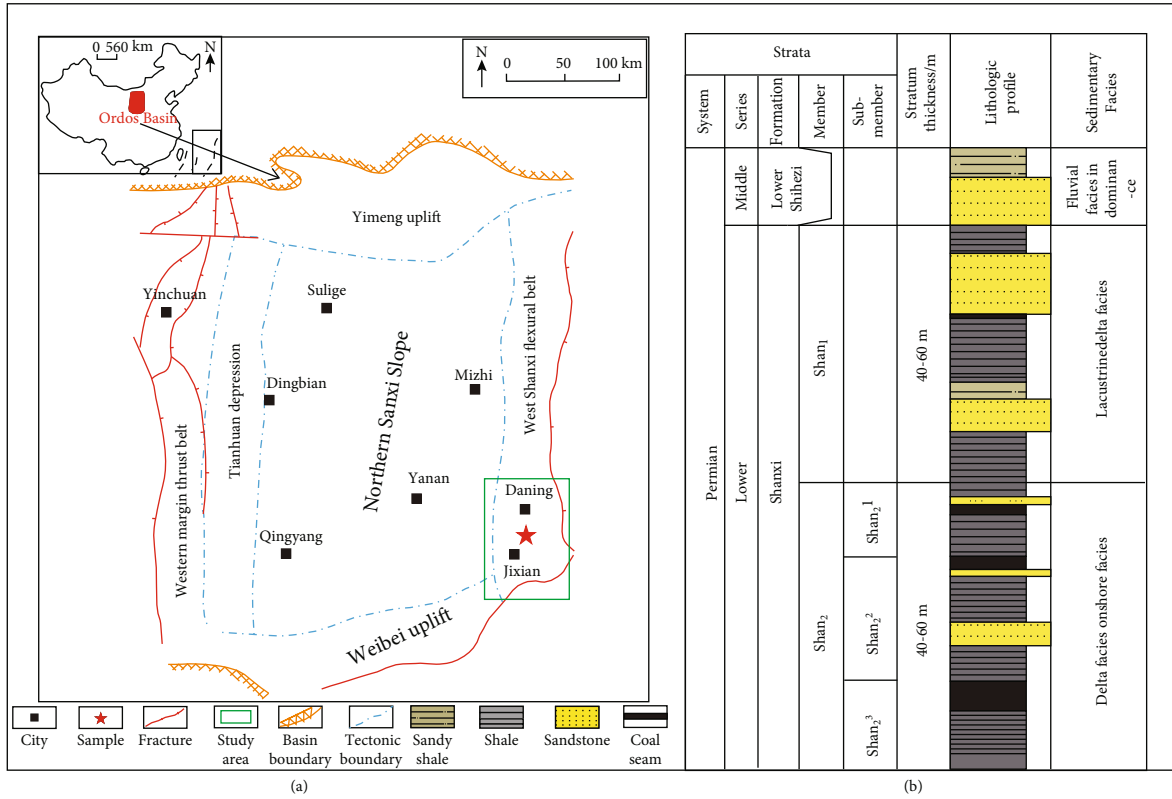


FIGURE 1: (a) Location of the study area. (b) Integrated strata of the Shanxi Formation in the Ordos Basin.

TABLE 1: Geochemical characteristics and mineralogical compositions of shale samples.

Samples	Depth (m)	Strata	TOC (%)	$R_o$ (%)	Relative percent (%)										
					Qu	Pl	Si	Ca	Do	Py	T C	I/S	I	K	Ch
Sample 1	2142.4	Shanxi	5.78	2.54	60.99	0.00	0.00	0.00	2.96	2.67	33.38	17.97	9.38	4.91	1.12
Sample 2	2143.2	Shanxi	6.43	2.33	59.74	0.00	0.00	0.00	3.83	2.79	33.63	15.34	11.07	5.50	1.72
Sample 3	2144.4	Shanxi	11.1	2.37	48.79	0.00	0.00	1.68	4.90	3.88	40.75	21.73	8.32	9.25	1.44
Sample 4	2145.2	Shanxi	8.66	2.17	37.87	0.00	0.00	11.01	2.55	4.26	44.31	19.17	9.81	14.43	0.90
Sample 5	2148.9	Shanxi	7.83	2.38	59.68	0.00	0.00	0.00	1.32	0.00	39.00	13.03	6.64	17.36	1.98
Sample 6	2150.9	Shanxi	1.82	2.08	31.12	2.48	4.71	0.00	0.00	0.34	61.35	13.03	14.98	30.18	3.16
Sample 7	2152.6	Shanxi	1.08	2.16	37.74	0.00	5.73	0.00	0.00	3.46	53.06	13.03	26.81	10.79	2.44
Sample 8	2154.4	Shanxi	1.68	2.23	45.12	2.67	1.50	0.00	0.00	1.13	49.57	14.29	20.08	13.49	1.72
Sample 9	2158.6	Shanxi	1.84	2.19	36.03	1.71	2.56	0.00	1.27	0.63	57.80	14.54	19.99	19.48	3.79
Sample 10	2163.1	Shanxi	0.84	2.13	34.27	1.58	1.69	0.00	0.00	0.53	61.93	12.53	29.98	15.88	3.53
Sample 11	2165.9	Shanxi	2.37	2.36	38.00	3.99	1.12	0.00	0.00	1.11	55.78	13.03	20.37	20.06	2.32
Sample 12	2167.2	Shanxi	9.85	2.64	28.27	0.00	2.70	0.00	0.00	3.28	65.75	20.03	15.05	28.32	2.35

$R_o$  is the vitrinite reflectance; Qu, Pl, Si, Ca, Do, Py, and TC are the quartz, plagioclase, siderite, calcite, dolomite, pyrite, and total clays, respectively; I, I/S, K, and Ch are the illite, illite/smectite, kaolinite, and chlorite, respectively.

and origin: interparticle (inter P), intraparticle (intra P), and organic material (OM) pores [14, 15]. The irregularity of the pore structure and the random range of the pore size distribution are the major factors controlling gas storage and flow capacity [16, 17]. Numerous factors affect the pore structure of marine shale; however, mineral content is especially important for the generation and maintenance of pore structure

[18–20]. In addition, the content of OM is also an important factor affecting the development of shale pores, and the higher the content of OM is, the more favourable the development of micropores [21–24]. Due to the lack of study on marine to continental transitional shales, it is essential to appreciate the pore structure of these shales to assess shale reservoirs and understand how gas is stored and transported.

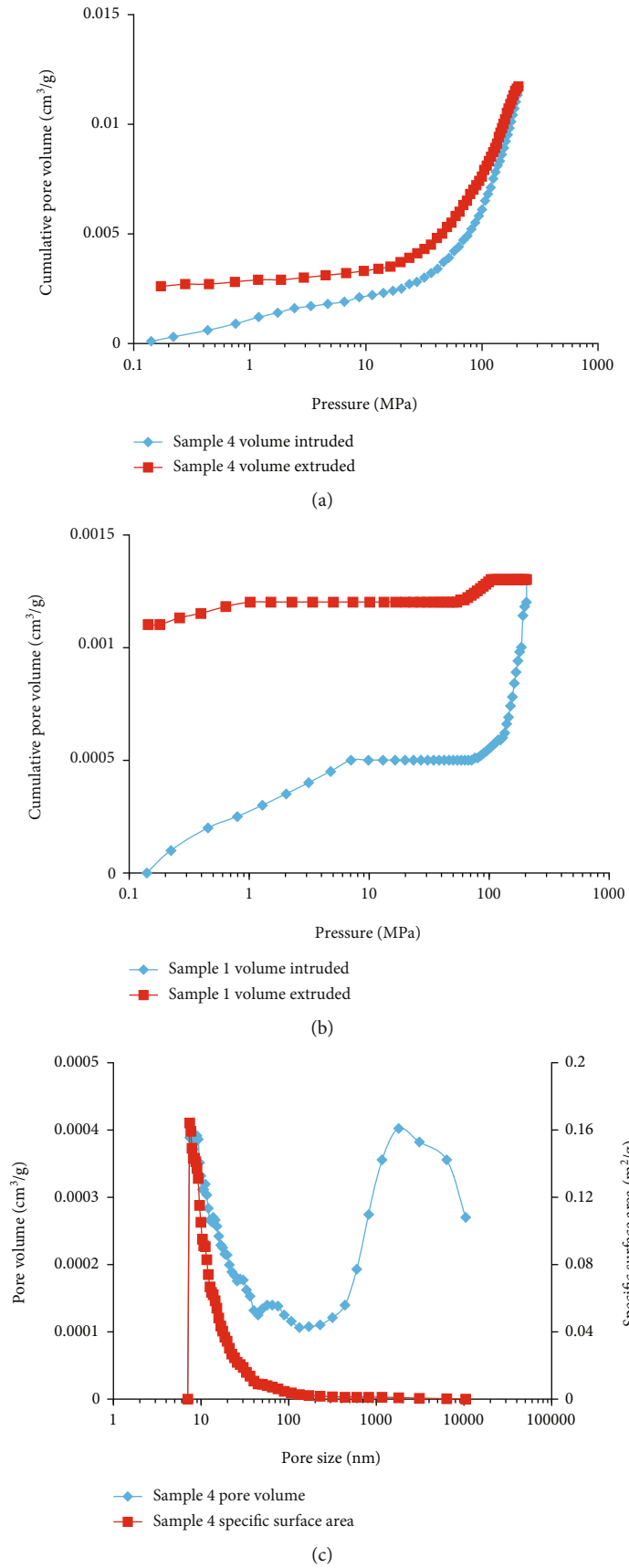


FIGURE 2: Continued.

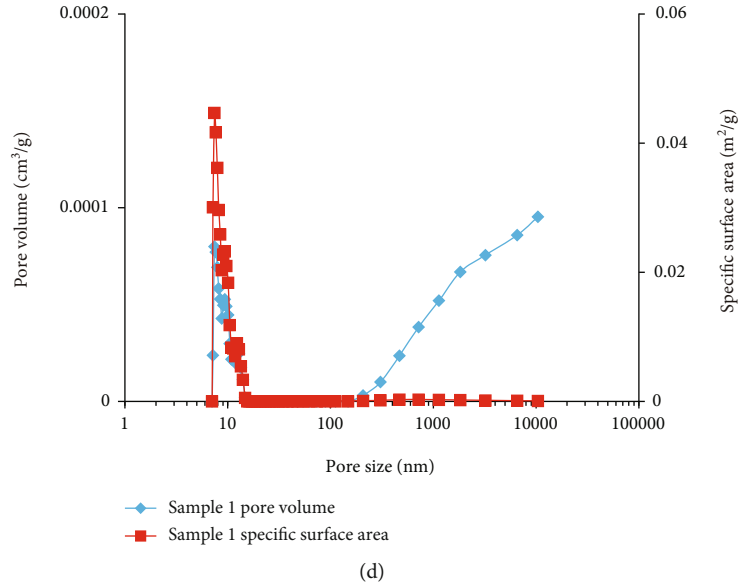


FIGURE 2: Typical sample mercury intrusion-extrusion curves and pore size distribution of samples.

In addition to conventional reservoir pore research methods, theoretical methods of porous material characterization are also introduced to pore characteristics of shale, which can be roughly summarized as image analysis, fluid injection method, and nonfluid injection method [25–29]. Image analysis techniques such as scanning electron microscopy [25, 30], field emission scanning electron microscopy [31, 32], focused ion beam scanning electron microscopy [33], transmission electron microscopy, and atomic force microscopy can be used to intuitively observe and analyse the morphology and size of microscopic pores in shale [30–35]. Fluid injection techniques, such as high-pressure mercury injection (HPMI) [25], low-temperature  $N_2$  adsorption (LT- $N_2$ GA) [32, 33], low-pressure  $CO_2$  adsorption (LP- $CO_2$ GA) experiments [32, 33], and He-Hg pore analysis experiments, have been used [31–33, 36–38]. A series of nonfluid injection techniques, such as low-field nuclear magnetic resonance [39], small-angle/ultras-small-angle neutron scattering [40, 41], and micro- and nano-CT scanning, have been used to quantitatively characterize and analyse shale nanopore structures [35, 38–43]. Low-pressure gas adsorption is the simplest and most common of these experimental methods. While LT- $N_2$ GA and HPMI are useful for studying mesopores and macropores, LP- $CO_2$ GA has been demonstrated to be a more effective method for determining the structure of micropores [25, 31–33, 36, 37].

Recent study indicating about  $1.9 \times 10^{12} m^3$  of saturated gas resources in the Upper Carboniferous demonstrates the tremendous development prospects of shale gas in Carboniferous and Permian transition shale reservoirs on the eastern margin of the Ordos Basin [7–9]. In addition, Li et al. found that the coal-bearing strata on the eastern margin of the Ordos Basin have a significant potential for the coproduction of tight sand gas, shale gas, and coalbed methane [12]. This analysis focuses primarily on twelve shale samples from the Permian Shanxi Formation on the eastern margin of the

Ordos Basin. Considering the differences in determination effectiveness of different test methods for shale porosity, we obtained the pore size distribution (PSD), from nanopores to micropores, of the shale in the study area through LP- $CO_2$ GA, LT- $N_2$ GA, and HPMI. We investigated the influence of the abundance, organic matter maturity, and mineral composition on shale pore development through TOC and whole-rock mineral X-ray diffraction analysis. These results, combined with high-pressure methane adsorption (HPMA) experiment results, were then used to discuss the influence of the complete pore structure on the adsorption capacity of shale. Consequently, our research serves as a guide and point of reference for the finding and exploitation of shale gas in the Shanxi Formation along the eastern margin of the Ordos Basin and adjoining basins.

## 2. Geological Setting

The Ordos Basin is around  $37 \times 10^4 km^2$  in size and almost rectangular in form. Based on the existing tectonic features [12, 44], according to the structural morphology, the basin can be subdivided into six subtectonic units (Figure 1(a)). The study area is located on the eastern margin of the Ordos Basin, the structure is relatively stable, the stratigraphy is monoclinical to the west, and the outcropping layers are young from east to west [8, 9, 12]. After the Early Ordovician, during the influence of the Caledonian movement, the sedimentary thickness of the inner layer of the basin decreased, and then, the basin was fully uplifted and denuded. Carboniferous and Permian transitional strata were extensively deposited, including the upper Carboniferous Benxi formations, and the lower Permian Taiyuan Formation and Shanxi Formation were deposited (Figure 1(b)) [9]. The sedimentary tectonic evolution of the Ordos Basin and the stratigraphic characteristics of the studied region are intricately interwoven. The basin, as well as the whole

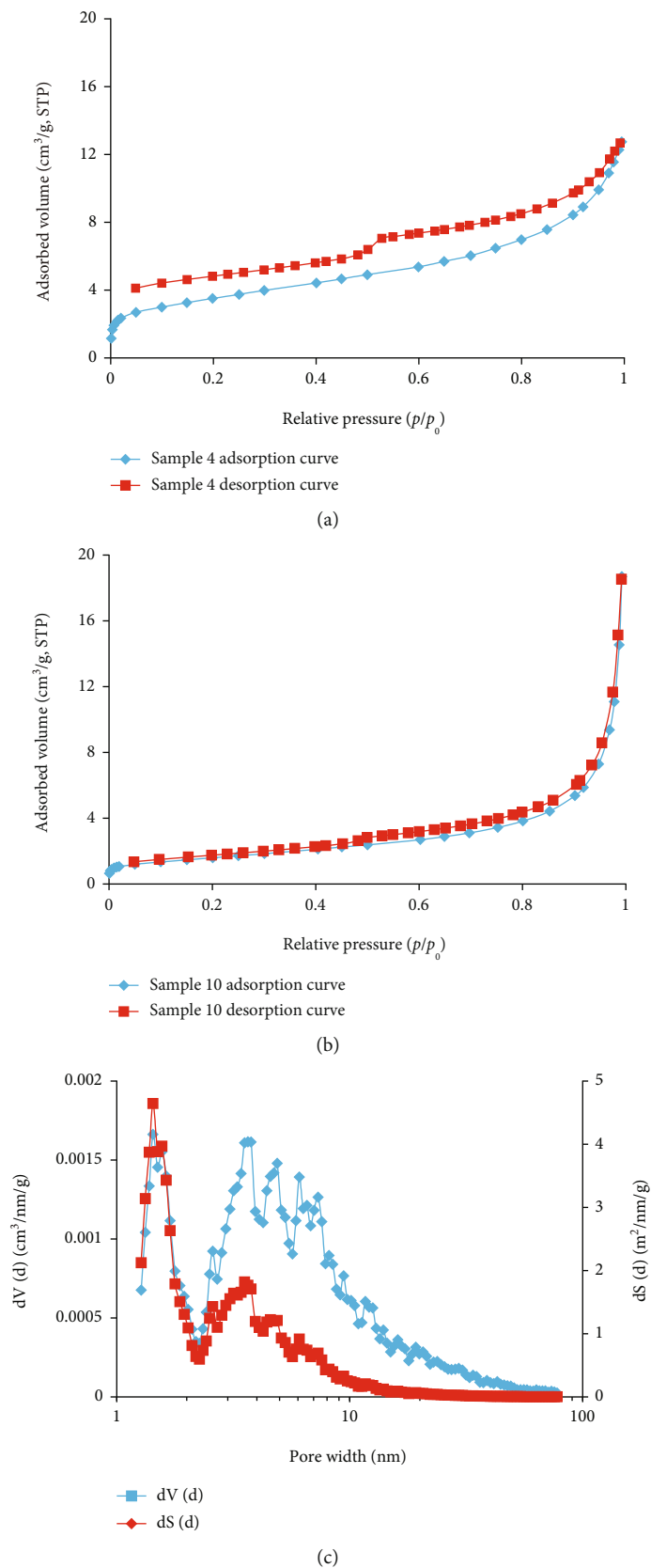


FIGURE 3: Continued.

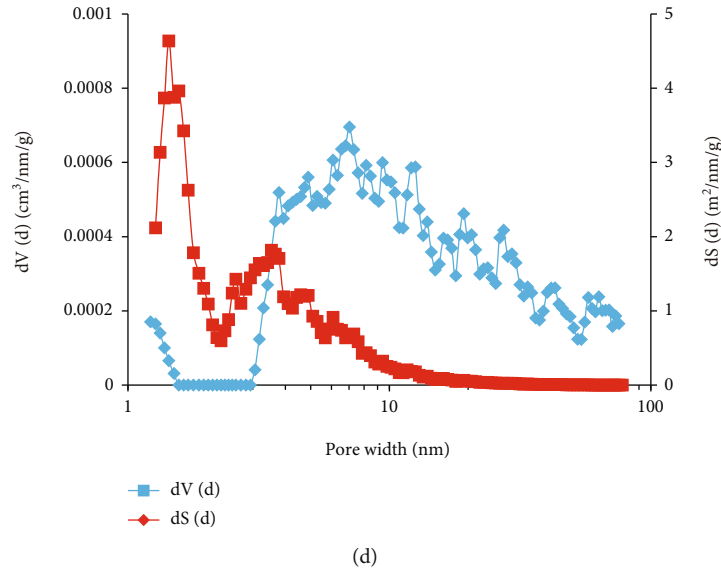


FIGURE 3: Typical sample  $N_2$  adsorption-desorption isotherms and pore size distribution of samples.

TABLE 2: Pore types obtained from the adsorption isotherms using  $N_2$  adsorption-desorption isotherms.

Loop type	Sample	Pore type
H3	Sample 1, sample 6, sample 7, sample 8	Plate-shaped pore
	Sample 9, sample 10, sample 11, sample 12	Wedge-shaped tubular pore
		Parallel slit-shaped pore
H4	Sample 2, sample 3, sample 4, sample 5	Plate-shaped pore Ink bottle-shaped pore

Great North China Block, experienced a facies sequence evolution history from a marine environment with sea-land interaction to an inland lake basin in the period from the Benxi Period of the late Palaeozoic to the Shiqianfeng Period of the late Permian [8]. Due to regional tectonic activity, the water body changed periodically, forming multiple stage sedimentary phases of littoral shallow sea-delta front-littoral shallow lake facies and depositing many sets of marine to continental transition organic-rich shales [8, 9].

### 3. Samples and Methods

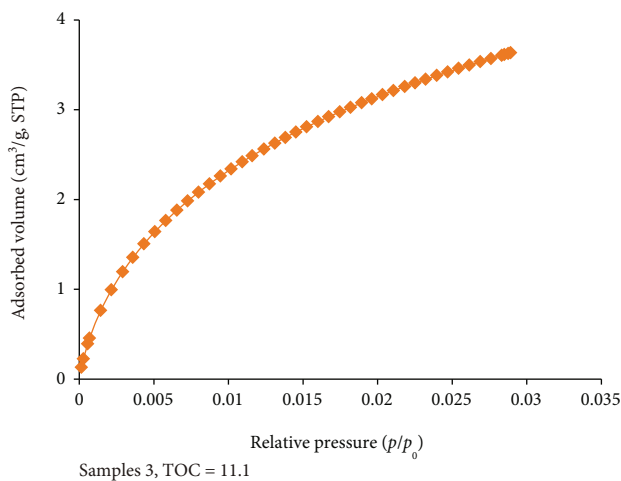
**3.1. Samples.** The experimental samples used in this study were all extracted from shale gas well cores and came from the Shanxi Formation on the eastern margin of the Ordos Basin. Twelve shale samples with different TOC contents were selected to conduct experiments on LP- $CO_2$ GA, LT- $N_2$ GA, HPMI, and HPMA.

**3.2. TOC, Thermal Maturity, and Mineral Component.** Shale samples were first treated with HCl to remove carbonate, then rinsed with deionized water to remove any leftover HCl, and then dried at  $110^\circ C$  for 12 hours. The TOC content was measured by a LECO CS230 carbon/sulfur analyser in line with national standard GB/T19145-2003. Cutting samples were made into pellets and then ground and polished. Before measuring the samples, the MPV-II microphotome-

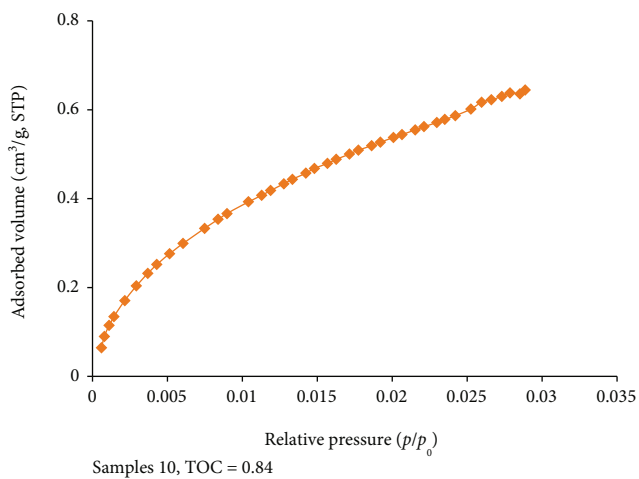
ter was calibrated via the twofold calibration technique in order to measure the vitrinite reflectance. Two reference samples were selected so that the gadget could be repeatedly calibrated until it reached its optimal state [45, 46]. In accordance with the Chinese Oil and Gas Industry Standard SY/T 5124-2012, measuring points were evenly distributed across sample surfaces to ensure measurement accuracy. The mineral compositions of the shale samples were determined by using Bruker D8 Advance X-ray diffractometers [46]. The minerals and the relative mineral percentages for each sample were estimated following the Chinese Oil and Gas Industry Standard SY/T 5163-2018.

**3.3. High-Pressure Mercury Intrusion (HPMI) Porosimetry.** The HPMI test was carried out by the Autopore-9505 mercury intrusion tester following national standards GB/T 21650.1-2008, which measured apertures between 3.6 nm and  $960 \mu m$ , with a maximum pressure of 60,000 psi (413 MPa) and a volumetric accuracy of less than  $0.01 \text{ cm}^3$ . Samples were heated in a vacuum oven at 3 Pa and  $105^\circ C$  for 16 h to remove moisture, and then, the samples were evacuated before mercury injection. The pore diameter distribution was obtained according to the Washburn formula [47].

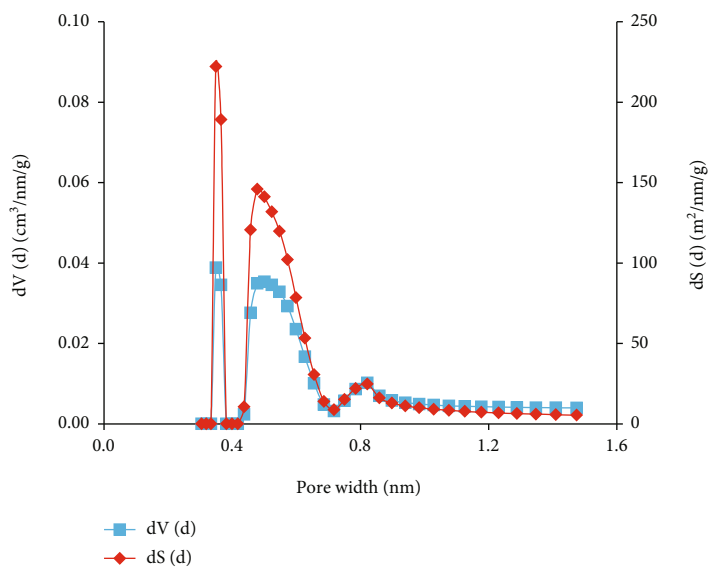
**3.4. Low-Pressure Gas Adsorption Experiments.** Using the gas adsorption approach, the nanopore distribution in shale may be successfully determined. Micropores are often



(a)



(b)



(c)

FIGURE 4: Continued.

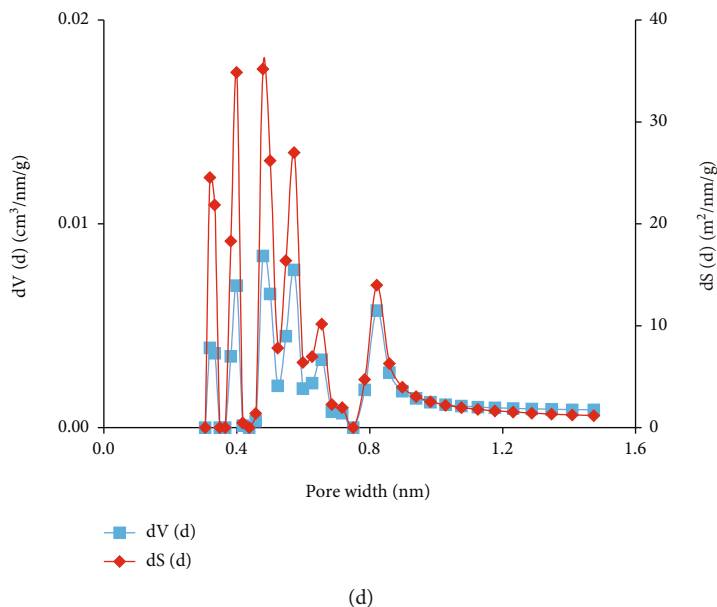


FIGURE 4: Typical sample CO<sub>2</sub> adsorption isotherms and pore size distribution of samples.

examined by LP-CO<sub>2</sub>GA, while mesopores may be examined by LT-N<sub>2</sub>GA.

LT-N<sub>2</sub>GA and LP-CO<sub>2</sub>GA analysis was carried out using a Quantachrome Autosorb-IQ specific surface area and micropore analyser, in accordance with the national standards GB/T 21650.2-2008 and GB/T 21650.3-2011. Its limit of SSA is 0.0005 m<sup>2</sup>/g, its range of pore diameter is from 0.35 nm to 500 nm, and its PV limit is 0.0001 cm<sup>3</sup>. All the samples were subjected to vacuum at 105°C for 12 h to remove the water and volatile substances in the samples. The LT-N<sub>2</sub>GA experiment was performed at 77 K with a nitrogen purity greater than 99.999%. The SSA was obtained by using the Brunauer-Emmett-Teller (BET) methods, and the PV and PSD were calculated by the density functional theory (DFT) model [48]. The LP-CO<sub>2</sub>GA experiment was performed at different partial pressures at 273 K. The PV, SSA, and PSD of the micropores (<2 nm) are calculated by a more suitable DFT model.

**3.5. High-Pressure Methane Adsorption (HMPA).** The HMPA experiments were performed by a Gravimetric Isotherm Rig 3 instrument with a temperature accuracy of 0.5°C and a high-precision accuracy of 0.1%. This equipment was from the CNPC Key Laboratory of Unconventional Oil & Gas. The methane adsorption experiment was conducted under a fixed temperature of 70°C and a pressure ranging from 0 MPa to 25 MPa. Following the shale samples' crushing to a mesh size of 60-80, around 100 g of each sample was put into the sample cell and put through a seal test and then underwent a methane adsorption test in accordance with the Chinese standard GB/T 19560-2008.

## 4. Results

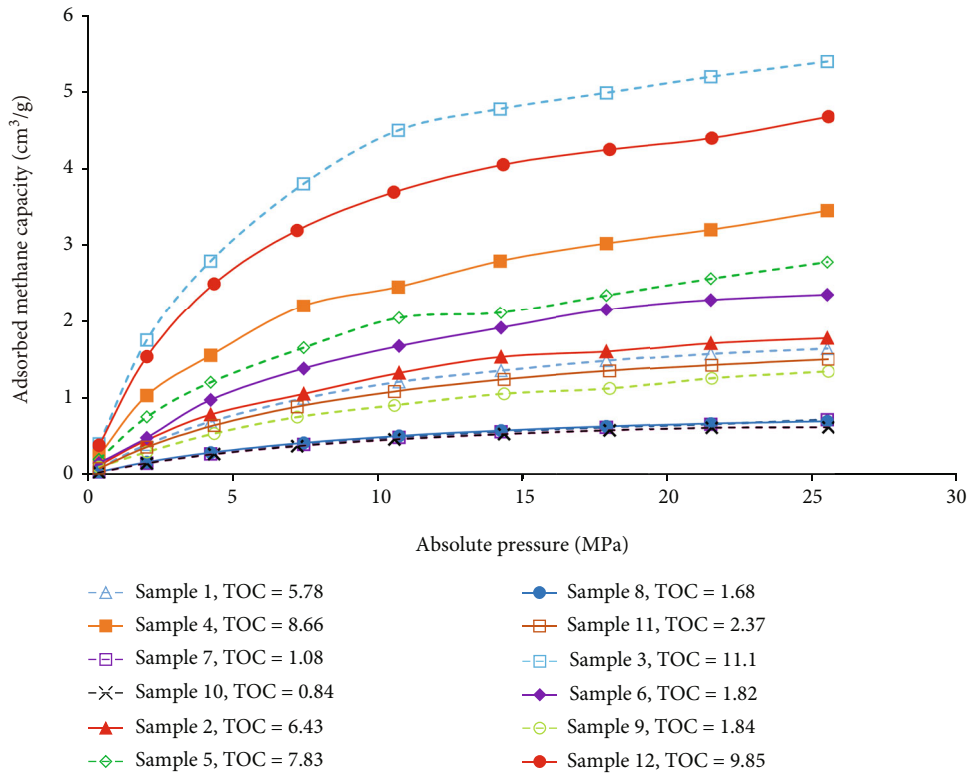
**4.1. Organic Geochemistry and Petrology.** The TOC contents range from 0.84% to 11.1% (mean 4.94%) (Table 1). The

shales are generally the stages of late high mature to early overmaturity, and the vitrinite reflectance ( $R_o$ ) ranged from 2.08% to 2.64% (mean 2.30%). The mineral contents of the shale samples varied (Table 1). The clay mineral content is the highest, ranging from 33.38% to 65.75% (mean 49.69%); the quartz content is the second-highest, with an average of 43.14%, and the shales also contain feldspar, calcite, dolomite, pyrite, and other minerals [41]. The clay minerals are mainly illite and I/S mixed layer with a minor amount of kaolinite and chlorite.

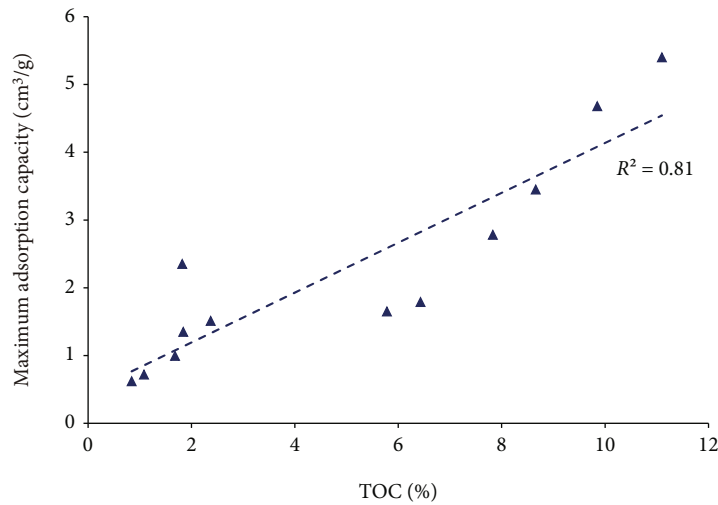
**4.2. Pore Structure Determined by Mercury Porosimetry (HPMI).** HPMI curves can reflect the development and connectivity of pores in different pore-throat segments [37, 49, 50]. Based on the mercury intrusion and extrusion curves, Figure 2 depicts two unique types of pore architecture (A and B). Type A, represented by sample 4, represents fully open pores with good connectivity and can be described as cylinder-like pores. The pore morphology of type B, represented by sample 1, is mainly that of half-open pores with poor connectivity, similar to that of slit- and plate-like pores.

The mercury intrusion and extrusion curves of some samples are shown in Figures 2(a) and 2(c), showing the typical two-stage pattern represented by sample 4. Such curves have high mercury extrusion efficiency, which indicates that there are more open pores and that the pore connectivity is good [49, 50]. The mercury intrusion and extrusion curves of the other shale samples are shown in Figures 2(b) and 2(d), showing a typical three-section pattern, represented by sample 1. However, such curves have a low mercury extrusion efficiency, indicating that the open pores in the mercury injection test aperture range are smaller and the pore connectivity is worse [50].

**4.3. Pore Structures by Low-Temperature N<sub>2</sub> Adsorption (LT-N<sub>2</sub>GA).** HPMI cannot accurately characterize the mesopores



(a)



(b)

FIGURE 5: (a) Isothermal adsorption curves of shale samples and (b) the interrelationship between TOC content and maximum adsorption capacities.

in shale samples [51]; therefore, a LT-N<sub>2</sub>GA experiment is used to characterize the mesopores. The nitrogen gas adsorption-desorption isotherms are as follows (Figure 3). According to the IUPAC, four types of hysteresis loops are classified [13]. The nitrogen gas adsorption-desorption isotherms show two types of pore structures, H3 and H4 (Table 2).

From the hysteresis loops formed (Figure 3(a)), represented by sample 4, the corresponding nitrogen gas adsorption-desorption isotherm rises slowly in the medium-

low-pressure section and rapidly in the high-pressure section. There is no obvious saturated adsorption platform in the adsorption branch. The desorption branch decreases slowly at the beginning, decreases rapidly in the medium-pressure section, and finally decreases slowly again. This pattern is generally consistent with the characteristics of H4-type hysteresis loops and indicates that the pore morphology is generally characterized by parallel slit-, plate-, and ink bottle-shaped pores. According to the massive hysteretic loops of these pores (Figure 3(c)), the shale pores consist of a large

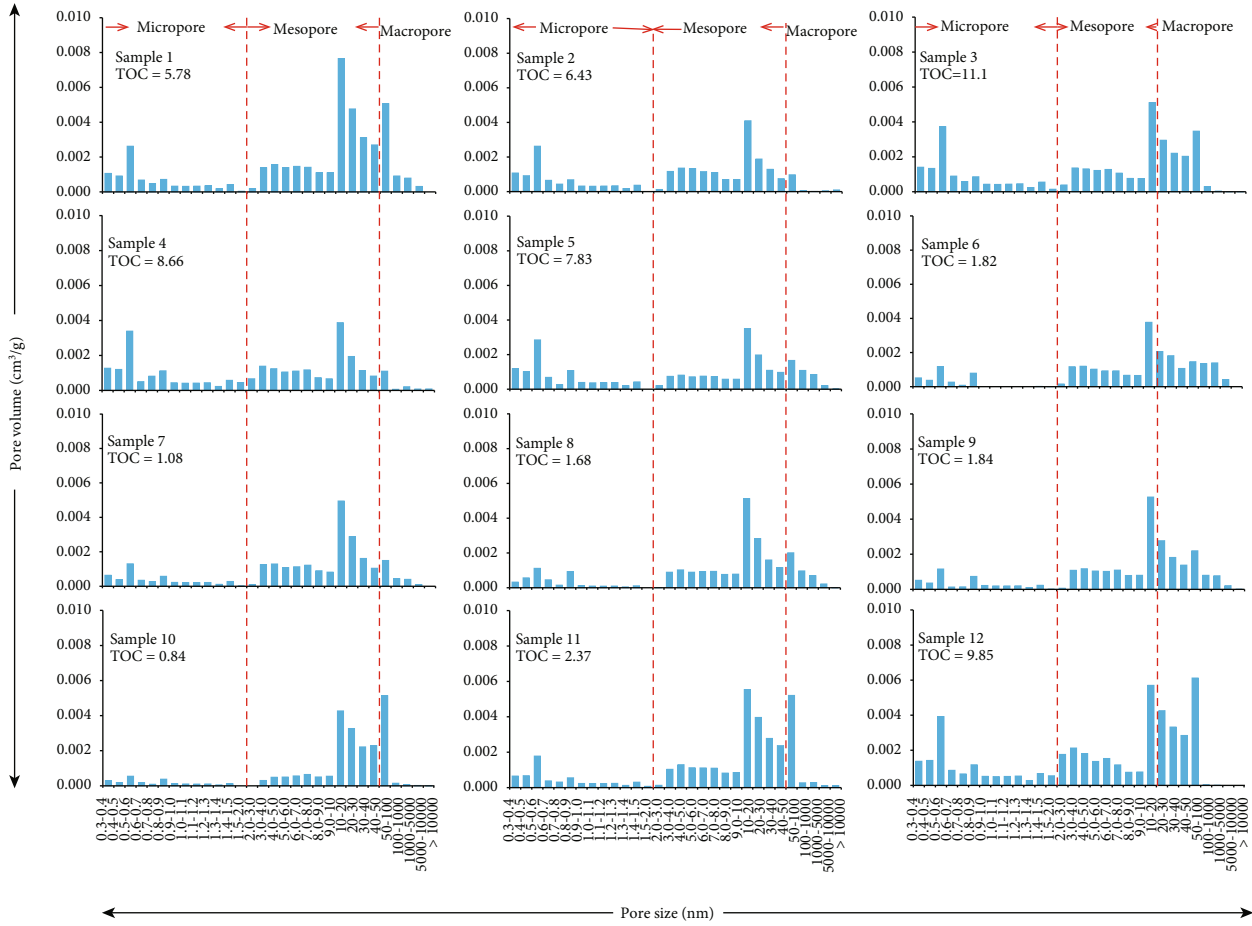


FIGURE 6: Histogram of complete PV distribution of shale samples.

TABLE 3: Statistical results of pore volume of shale samples.

Sample ID	PV ( $10^{-3} \text{ cm}^3/\text{g}$ )			Total	Proportion (%)		
	Micropore	Mesopore	Macropore		Micropore	Mesopore	Macropore
Sample 1	8.41	27.81	7.07	43.30	19.42	64.24	16.34
Sample 2	8.24	15.67	1.19	25.09	32.82	62.43	4.75
Sample 3	11.47	20.43	3.82	35.72	32.12	57.19	10.69
Sample 4	11.27	15.81	1.54	28.62	39.37	55.24	5.38
Sample 5	9.24	12.68	3.82	25.74	35.89	49.26	14.86
Sample 6	3.22	15.45	4.63	23.30	13.83	66.31	19.86
Sample 7	4.79	18.30	2.43	25.52	18.78	71.71	9.51
Sample 8	4.10	16.94	3.89	24.92	16.43	67.96	15.61
Sample 9	4.17	18.30	3.99	26.45	15.76	69.17	15.07
Sample 10	2.25	15.60	5.38	23.23	9.69	67.15	23.16
Sample 11	5.77	22.42	5.99	34.17	16.88	65.61	17.52
Sample 12	12.96	27.43	6.16	46.54	27.84	58.93	13.23

PV is the pore volume.

number of micropores and a small number of mesopores. In terms of the hysteric loops formed by other shale samples (Figure 3(b)), represented by sample 10, the corresponding adsorption isotherm increases slowly in the middle- and low-pressure sections and rapidly in the high-pressure sec-

tion, and the isotherm is nearly vertical. The desorption branch and the adsorption branch are nearly parallel in the high-pressure section and exhibit a steep near-vertical pattern. The middle- and low-pressure sections have a gentle trend, and the adsorption branch overlaps the desorption

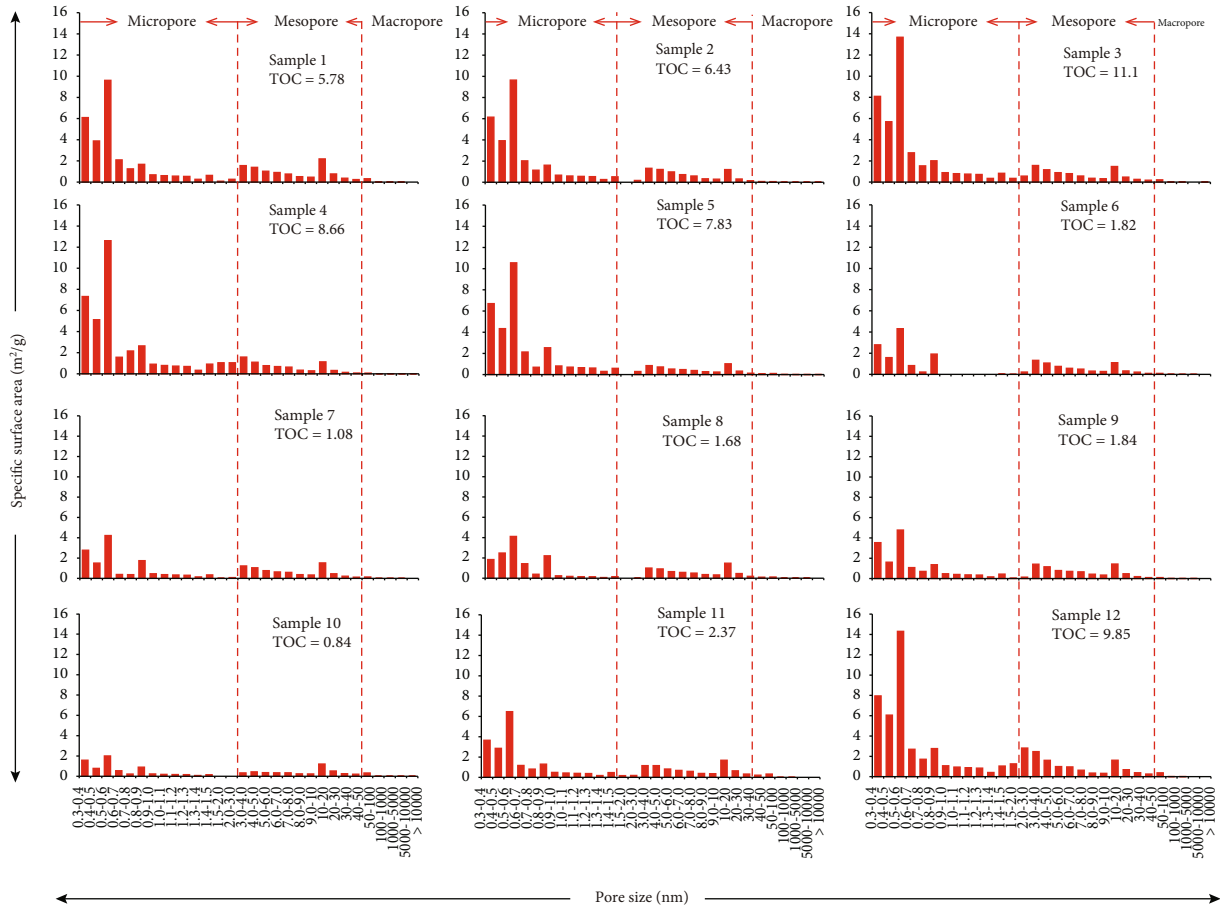


FIGURE 7: Histogram of complete SSA distribution of shale samples.

TABLE 4: Statistical results of specific surface area of shale samples.

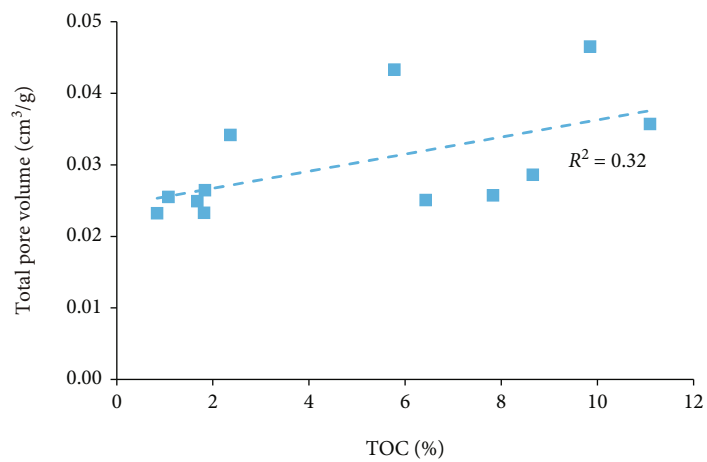
Sample ID	SSA (m <sup>2</sup> /g)			Total	Proportion (%)		
	Micropore	Mesopore	Macropore		Micropore	Mesopore	Macropore
Sample 1	28.02	10.48	0.33	38.83	72.16	26.98	0.86
Sample 2	27.62	7.36	0.06	35.04	78.82	21.00	0.18
Sample 3	38.50	8.63	0.23	47.36	81.30	18.23	0.48
Sample 4	36.88	8.12	0.07	45.08	81.82	18.02	0.16
Sample 5	30.64	5.34	0.12	36.11	84.86	14.80	0.34
Sample 6	11.72	6.80	0.12	18.63	62.90	36.48	0.62
Sample 7	15.32	7.83	0.10	23.25	65.87	33.69	0.44
Sample 8	13.45	6.60	0.14	20.20	66.60	32.69	0.70
Sample 9	12.98	7.37	0.15	20.50	63.30	35.95	0.74
Sample 10	7.05	4.50	0.33	11.88	59.35	37.90	2.75
Sample 11	18.81	8.22	0.33	27.36	68.74	30.05	1.21
Sample 12	41.97	13.12	0.38	55.47	75.65	23.66	0.69

SSA is the special surface area.

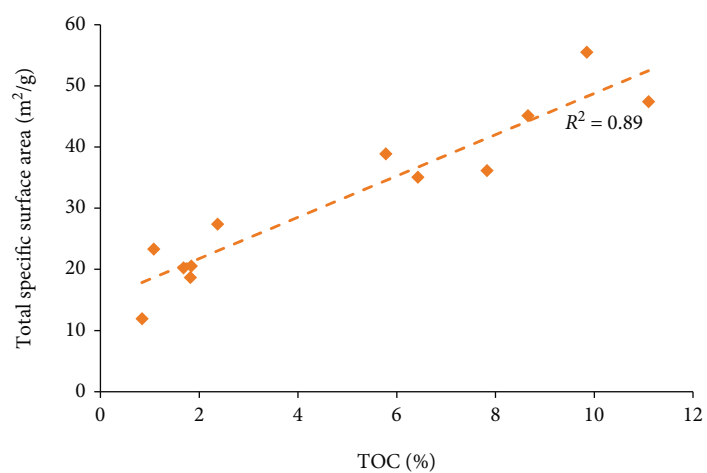
branch. This pattern is similar to that of the H3-type hysteric loop and indicates that the pore morphology is dominated by plate-shaped pores and wedge-shaped tubular pores. In addition, this pattern demonstrates that the shale pores are well-connected and sizable (Figure 3(d)). The shale of the Shanxi Formation in the study area has a very complex

pore structure that is often irregular and consists of plate-shaped pores, ink bottle-shaped pores, and wedge-shaped tubular pores [51].

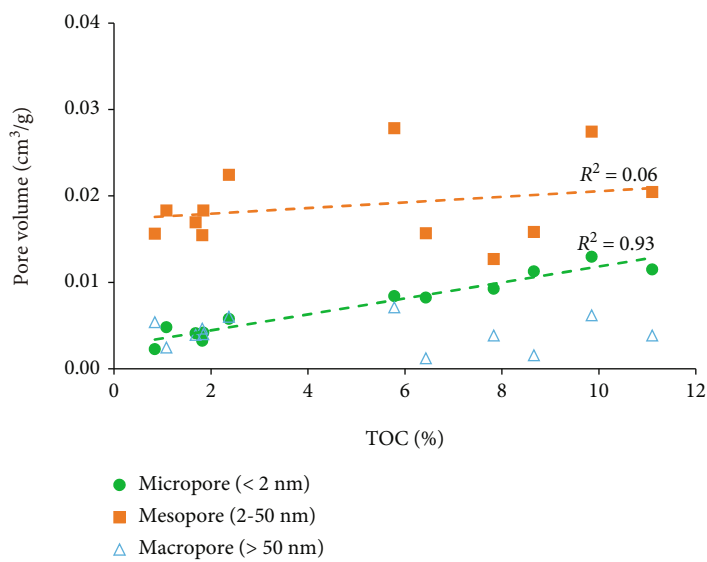
4.4. Pore Structures by Low-Pressure CO<sub>2</sub> Adsorption (LP-CO<sub>2</sub>GA). CO<sub>2</sub> molecules may measure pore widths in the



(a)

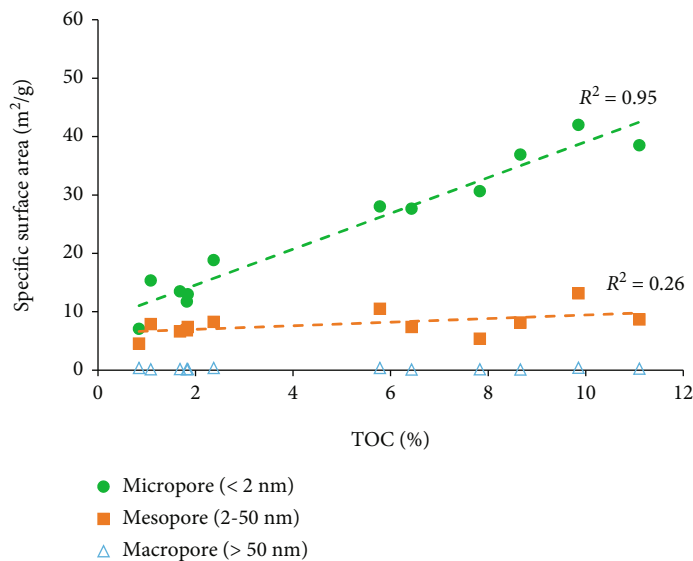


(b)



(c)

FIGURE 8: Continued.



(d)

FIGURE 8: Cross-plots of TOC content with (a) total PV, (b) total SSA, (c) PV, and (d) SSA.

range of 0.3 to 2.0 nm at high temperatures (273 K) owing to their advantageous properties, such as high energy and rapid balancing [50, 51]. Figures 4(a) and 4(b) show that the LP-CO<sub>2</sub>GA isotherms are type I at low temperatures. In the low-pressure region ( $p/p_0 < 0.01$ ), the adsorption quantity is small but the rate is high, and as the relative pressure is increased, the adsorption quantity continuously increases while the rate progressively drops. Overall, the adsorption capacity increased significantly with increasing TOC content in the 12 samples. The adsorption capacity of sample 3 is the largest, greater than 3.5 cm<sup>3</sup>/g, indicating that it contains many micropores. Sample 10 has the lowest adsorption capacity, less than 1.0 cm<sup>3</sup>/g, indicating that the sample contains a few micropores. According to the DFT model, the PSD curve of sample 3 comprises three peaks, the bulk of which are scattered between 0.3 and 0.8 nm (Figure 4(c)). The PSD curve for sample 10 displays six peaks (Figure 4(d)), the bulk of which are dispersed between 0.35 and 0.7 nm and 0.75 and 0.9 nm, indicating that the majority of the micropores are distributed between these pore size ranges.

**4.5. Adsorption Capacity from High-Pressure Methane Adsorption (HPMA).** HPMA experiments can test the maximum CH<sub>4</sub> adsorption capacity of shale under fixed temperature and pressure conditions [52]. As Figure 5(a) shows, under the conditions of 25 MPa and 70°C, the maximum CH<sub>4</sub> adsorption capacity of the Shanxi Formation shale after balanced water treatment is significantly different. The maximum adsorption capacities of shale samples are between 0.62 cm<sup>3</sup>/g and 5.40 cm<sup>3</sup>/g (mean of 2.27 cm<sup>3</sup>/g). The maximum CH<sub>4</sub> adsorption capacities of sample 3 and sample 10 are 5.40 cm<sup>3</sup>/g and 0.64 cm<sup>3</sup>/g, and the corresponding TOC contents are 11.1% and 0.84%, respectively. The maximum CH<sub>4</sub> adsorption capacity of shale tends to increase with the increase in total organic carbon content (Figure 5(b)), and the correlation coefficient is as high as 0.81, indicating that

organic carbon content is the main factor affecting the development of nanoscale pores in shale. With the increase in TOC content, CH<sub>4</sub> adsorption capacity of shale also increases, which is consistent with previous research results [52–55]. The reason may be that the increase in shale thermal evolution makes kerogen generate hydrocarbon and form more organic pores. In addition, OM pores have a greater internal pore SSA than other types of pores. As a consequence, the increase in TOC content provides a large amount of storage space for shale gas, thus increasing the overall gas content.

## 5. Discussion

**5.1. Complete Pore Structure Characteristics.** Due to the complex and variable pore structure of shale and the vast range of pore diameters (from nanometer to micron development to varying degrees), it would be impossible for a single experimental approach to define the pores at all scales entirely and precisely. Based on the experimental results of HPMA, LT-N<sub>2</sub>GA, and LP-CO<sub>2</sub>GA [50, 51, 54, 56], the apertures of all pores in the Shanxi Formation shale on the eastern margin of the Ordos Basin are investigated. In this study, the best aperture measurement segments of these methods are selected for superposition analysis; among them, the micropores are characterized by LP-CO<sub>2</sub>GA experimental data, the mesopores are characterized by LT-N<sub>2</sub>GA experimental data, and the macropores are characterized by HPMA experimental data.

Using the aforementioned three procedures, the entire PSD properties of the Shanxi Formation shale samples in the study area were obtained. In terms of the PV distribution characteristics of the full pore size range, the PV distribution characteristics of different shale samples vary greatly, but in general, mesopores provide the majority of the PV, followed by micropores, and macropores provide a small amount of PV (Figure 6). In terms of specific data (Table 3), the total

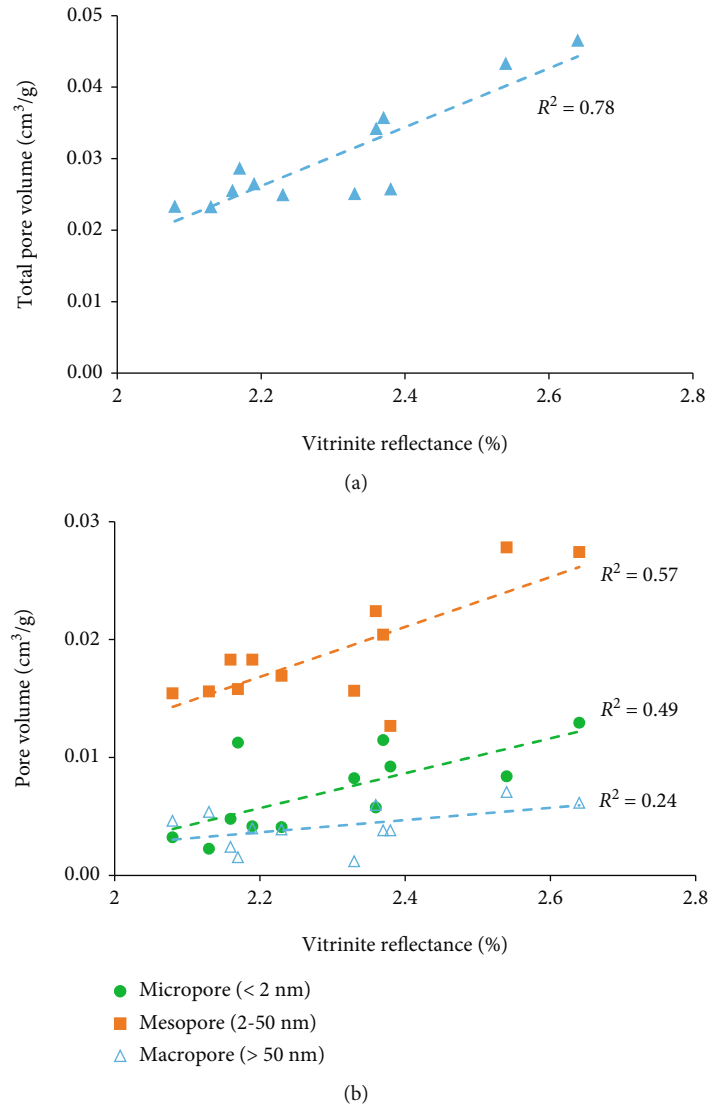


FIGURE 9: Cross-plots of vitrinite reflectance with (a) total PV and (b) PV.

PV of shale range from  $23.23$  to  $46.54 \times 10^{-3} \text{ cm}^3/\text{g}$  (mean  $30.22 \times 10^{-3} \text{ cm}^3/\text{g}$ ). The majority of micropores are formed between  $0.3$  and  $0.8 \text{ nm}$ , and the PV ranges from  $2.25$  to  $12.96 \times 10^{-3} \text{ cm}^3/\text{g}$  (mean  $7.16 \times 10^{-3} \text{ cm}^3/\text{g}$ ), accounting for  $9.69$ - $39.37\%$  of the total PV, with an average of  $23.24\%$ . The majority of mesopores are found in the pore size ranges of  $3$ - $6 \text{ nm}$  and  $10$ - $40 \text{ nm}$ , and the PV ranges from  $12.68$  to  $27.81 \times 10^{-3} \text{ cm}^3/\text{g}$  (mean  $18.90 \times 10^{-3} \text{ cm}^3/\text{g}$ ), accounting for  $49.26$ - $71.71\%$  of the total PV, with an average of  $62.93\%$ . The macropore volume is mainly contributed by pores above  $50$ - $100 \text{ nm}$ , whose value ranges from  $1.19$  to  $7.07 \times 10^{-3} \text{ cm}^3/\text{g}$  (mean  $4.16 \times 10^{-3} \text{ cm}^3/\text{g}$ ), accounting for  $4.75$ - $23.16\%$  of the total PV, with an average of  $13.83\%$ .

The analyses above have found that the pore types and structures of marine to continental transitional shale facies in the Shanxi Formation are quite different from those of marine shales in the Longmaxi formation. Jiang et al. and Shi et al. found that the PV of shale pores in Longmaxi Formation, Sichuan Province, is relatively developed in micro-

pores, mesopores, and macropores [51, 57]. Zhu et al. found that micropores, mesopores, and macropores all contribute to the PV of the Longmaxi formation shale in the Upper Yangtze region, and the contributions of micropores and macropores are more prominent [56]. In this paper, the pore volume of the marine to continental transitional shale in the Shanxi Formation is mainly provided by mesopores, while the contributions of micropores and macropores are lower. This difference is caused by the difference in organic matter types between marine shale and marine to continental transitional shale.

According to the distribution characteristics of the Shanxi Formation shale, the SSA area distribution of shale samples also has strong heterogeneity, and great differences exist among different samples. However, on the whole, micropores and mesopores provide most of the SSA, and the contribution of macropores to the SSA is minimal or even negligible (Figure 7). In terms of specific data (Table 4), the total SSA of the shale samples ranges from

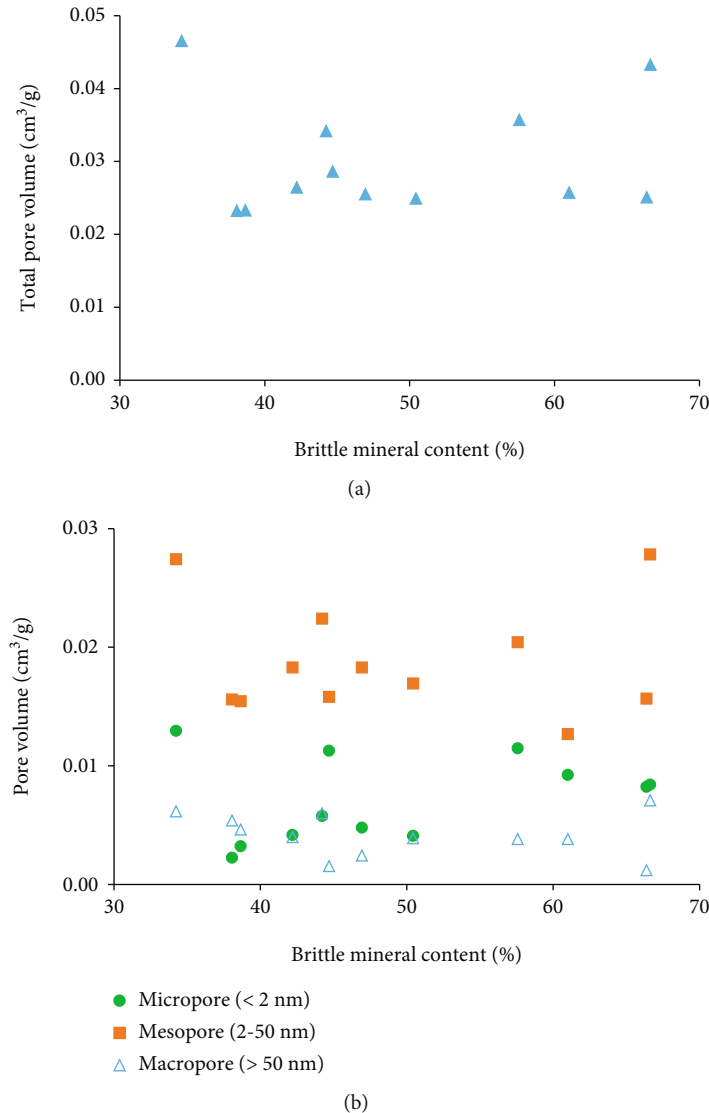


FIGURE 10: Cross-plots of brittle mineral content with (a) total PV and (b) PV.

11.88 to 55.47 m<sup>2</sup>/g (mean 31.64 m<sup>2</sup>/g). The bulk of the surface area specific surface area (SSA) of micropores is given by pores between 0.3 and 0.8 nm with values ranging from 7.05 to 41.97 m<sup>2</sup>/g (mean 23.58 m<sup>2</sup>/g), accounting for 59.35-84.86% of the total SSA, with an average of 71.78%. The SSA of mesopore is mainly provided by the mesopores in the range of 3-6 nm. The SSA of mesopores in the range of 10-40 nm in some samples ranges from 4.50 to 13.12 m<sup>2</sup>/g (mean 7.86 m<sup>2</sup>/g), accounting for 14.80-37.90% of the total SSA, with an average of 27.45%. The SSA ranges from 0.06 to 0.38 m<sup>2</sup>/g (mean 0.20 m<sup>2</sup>/g), accounting for 0.16-2.75% of the total SSA, with an average of 0.77%. This value range is consistent with that of the marine Longmaxi Formation shale [50, 51, 56, 57]. Because micropores consist of organic pores and clay pores, micropores offer a large adsorption space for shale gas.

5.2. Influencing Factors of Pore Structure. According to a number of researches [21-29, 51], the TOC content, the type

of organic material, and the mineral content of the clay have significant roles in controlling the PV and PSD of shale. Although different test methods and samples have been used, all the relevant studies show that the TOC content is the main controlling factor of micropores [23, 50-54, 58, 59].

5.2.1. Effect of TOC Content on Pore Structure. Organic material pores were formed predominantly from the heat decomposition of organic matter, which produced hydrocarbons [22, 29]. Numerous studies have shown that a high TOC content is advantageous for pore formation, the higher adsorption capacity, and the production of shale gas [25, 28, 51, 53, 58].

Figure 8(a) illustrates a weak linear relationship between the total PV and TOC content in the examined shale, indicating that the TOC content provides only part of the PV and that organic pores are not dominant. Figure 8(b) indicates that the SSA of shale does indeed have a significant positive correlation with TOC content, mainly because the

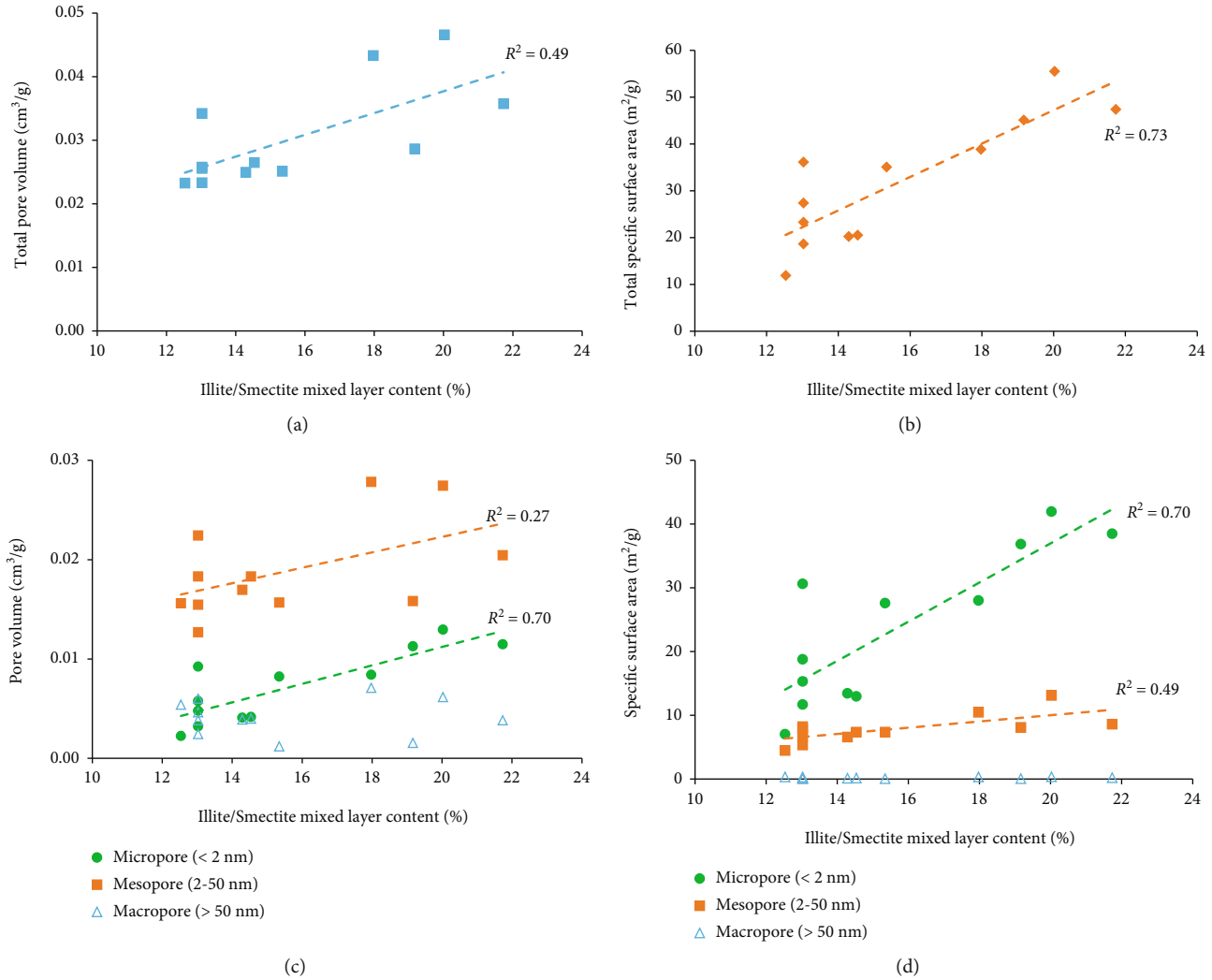


FIGURE 11: Cross-plots of illite/smectite mixed layer content with (a) total PV, (b) total SSA, (c) PV, and (d) SSA.

SSA of shale is mainly provided by micropores, and TOC content mainly controls the micropores. The TOC content has obvious positive correlations with the PV and SSA of micropores, with correlation values of 0.93 and 0.95, respectively (Figures 8(c) and 8(d)). However, the TOC content has no apparent relationships with the PV and SSA of mesopores and macropores. These results were consistent with those of most scholars [22, 25, 28, 29].

**5.2.2. Effect of Thermal Maturity on Pore Structure.** Some researchers have proposed that organic matter pores increase with organic matter maturation and that when the organic maturity of shale exceeds some threshold, the porosity of shale begins to decrease [28, 46, 60, 61].

The vitrinite reflectance ( $R_o$ ) of organic matter in the Shanxi Formation in the study area ranges from 2.08% to 2.64% (mean 2.30%). The total PV or the volume of micropores, mesopores, and macropores in the Shanxi Formation shale of the study area show an increasing trend with increasing  $R_o$  (Figures 9(a) and 9(b)). With the increase in  $R_o$ , the increase in the shale pore volume is not caused by the simultaneous increase in the pore

volume of all the micropores, mesopores, and macropores. Therefore, the maturity of  $R_o$  is an important factor affecting the development of shale pores in the Shanxi Formation.

### 5.2.3. Influence of Brittle Mineral Content on Pore Structure.

In the Shanxi Formation of the research region, quartz predominates the list of brittle shale minerals. The association between the volume of micropores, mesopores, and macropores or the total PV and the presence of brittle minerals is not visible, as shown in Figures 10(a) and 10(b). Brittle minerals host few micropores, and brittle mineral grains, such as quartz and calcite, have a low SSA [21, 45, 51]. Relative to the micropore SSA of the shale matrix, brittle minerals provide a negligible SSA. For mesopores and macropores, although the brittle mineral occurrence in mineral particles of mesopores and macropores has a certain protective effect, mesopores and macropores and a high content of shale matrix brittle minerals are not widely developed [51, 53]. Consequently, the relationships between the brittle mineral content and the total PV and mesoporous and macropore volume are not obvious.

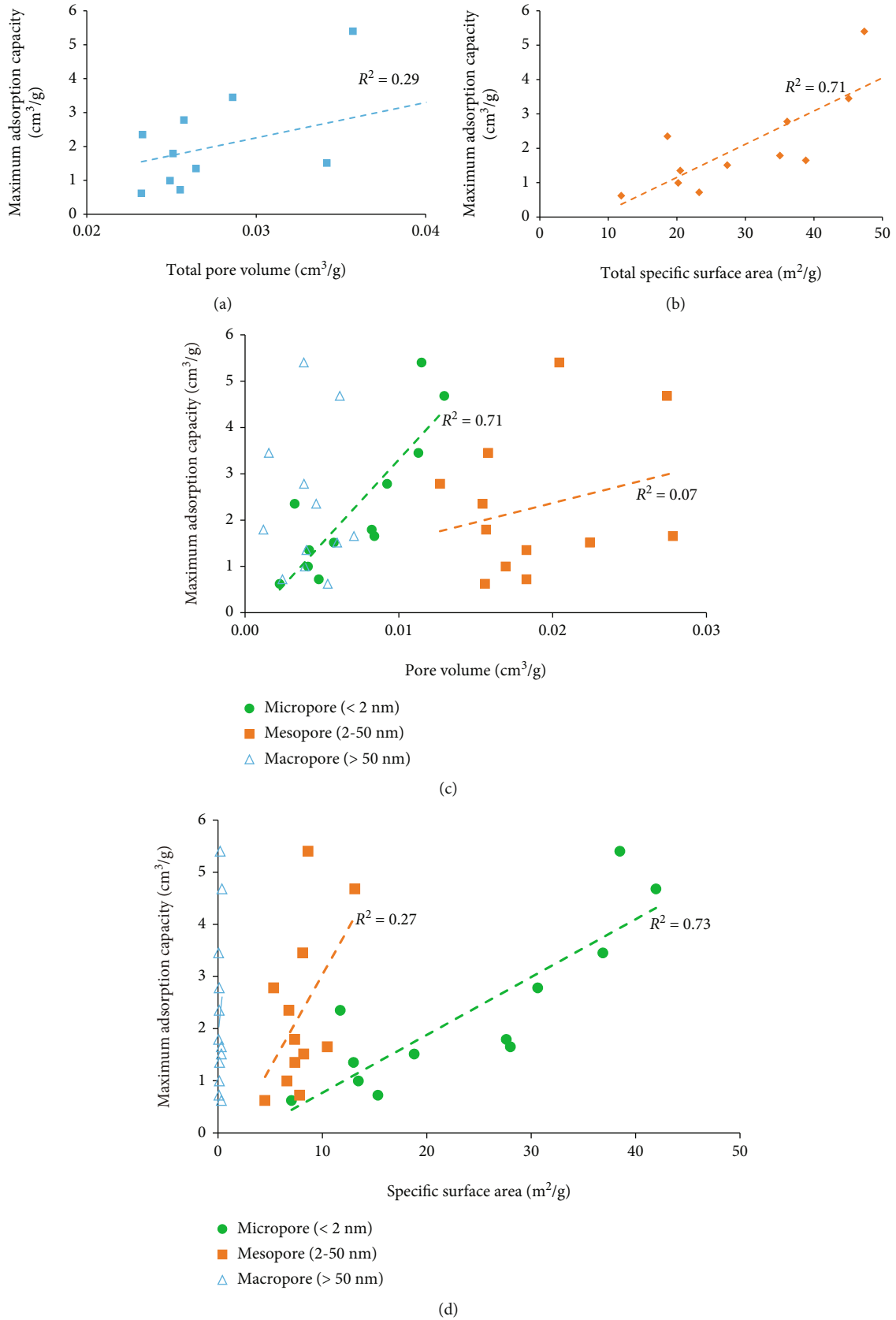


FIGURE 12: Cross-plots of maximum adsorption capacity with (a) total PV, (b) total SSA, (c) PV, and (d) SSA.

**5.2.4. Influence of Clay Minerals on Pore Structure.** Ross et al. found that different clay mineral components make different contributions to the PV and SSA of shale. Illite contributes the most, followed by montmorillonite, and chlorite contributes the least [14]. According to Passey et al., montmorillonite has an SSA of up to 800 m<sup>2</sup>/g, illite has just 30 m<sup>2</sup>/g, and kaolinite and chlorite have less than 15 m<sup>2</sup>/g [60].

As demonstrated in Figures 11(a) and 11(b), there are positive correlations between the I/S mixed layer content of shale samples and the total PV and total SSA. Consequently, the I/S mixed layer is the factor controlling the development of pore structure in the Shanxi Formation marine to continental transition shale. Figures 11(c) and 11(d) demonstrate that the quantity of illite/smectite mixed layer relates somewhat to micropore PV and SSA and moderately to mesopore PV and SSA, but there is no correlation with macropore PV and SSA, indicating that a certain amount of micropores and mesopores are developed in I/S mixed layer, which is not conducive to macropore development. The development of macropores is complex, and it is possible that the clay mineral content is too high and that rigid skeleton minerals are lacking, so compaction can easily lead to a decrease in macropores [14].

**5.3. PV and SSA on Methane Adsorption Ability.** In shale pores, only a limited quantity of shale gas exists in a dissolved form; the bulk is kept in adsorption and free states. Since the majority of free gas is contained in the pores or fractures of shale, PV and gas saturation essentially control the quantity of free gas. The majority of adsorption gas is adsorbed on the surface of organic matter (OM) and clay minerals, and the quantity of this gas is directly proportional to the SSA of shale [49, 51, 54]. As demonstrated in Figures 12(a) and 12(b), the maximum adsorption capacity of shale is positively connected with the PV and SSA, showing that the quantity of methane adsorption in shale samples steadily rises with increasing SSA. As demonstrated in Figures 12(c) and 12(d), the maximum adsorption capacity of shale samples is positively correlated with micropores, but the correlation of mesopores is poor, indicating that micropores SSA affected the amount of methane adsorption. The SSA provided by mesopores is limited and cannot play a decisive role in the amount of methane adsorption. The results show that micropores have a large SSA and control the adsorbed gas content of shale. The free gas volume is mainly determined by the PV of shale, the mesopores of shale pores in the Shanxi Formation play a dominant role in the total PV, and more free gas can be accommodated. Since macropores are mostly micron-scale pores, they may serve as the principal channel for shale gas migration, which is consistent with academic research done in China and worldwide on the adsorption capability of shale from various places [51, 54]. Chalmers et al. found that CH<sub>4</sub> adsorption in shales increases with the increase in micropore volume [16]. Zhong et al. found that the micropores of continental shale in Yanchang Formation had the most important influence on CH<sub>4</sub> adsorption capacity, and the correlation coefficient between micropores and adsorption capacity was significantly greater than other factors [61]. Lin et al. conducted

a large number of studies on marine shale of Longmaxi formation in Sichuan Basin and discovered that micropores are primarily responsible for shale's adsorption capacity [62].

## 6. Conclusions

- (1) Although shale contains micropores and macropores, mesopores predominate in the marine to continental transition Shanxi shale on the eastern edge of the Ordos Basin. The total SSA is 11.88~55.47 m<sup>2</sup>/g (mean 31.64 m<sup>2</sup>/g), and the total PV is 23.23~46.54 × 10<sup>-3</sup> cm<sup>3</sup>/g (mean 30.22 × 10<sup>-3</sup> cm<sup>3</sup>/g). Pores from 10 nm to 40 nm contribute most of the PV, and the SSA is mainly contributed by micropores < 0.8 nm
- (2) The maximum adsorption capacity in the marine to continental transitional Shanxi shale on the eastern margin of the Ordos Basin ranges from 0.62 cm<sup>3</sup>/g to 5.40 cm<sup>3</sup>/g (mean 2.27 cm<sup>3</sup>/g). With the increase in TOC content, the methane adsorption capacity of shale increases correspondingly, indicating that TOC has a strong adsorption capacity because organic pores can provide sufficient sites for gas adsorption
- (3) The TOC content, organic matter maturity, and I/S mixed layer contents are the main factors controlling the pore structure of transition shales in the Permian Shanxi Formation on the east margin of the Ordos Basin
- (4) The micropores of the Shanxi Formation shale have a large SSA and control the gas adsorption, the mesopores provide the main PV and the space for free gas, and the macropores form the main migration channels for gas

## Data Availability

The data are available upon request.

## Conflicts of Interest

The authors declare that they have no conflicts of interest.

## Acknowledgments

This research was jointly supported by the National Natural Science Foundation of China (Grant No. 41472122) and Innovative Team Project of Hubei Provincial Department of Education (Grant No. T201905). We thank PetroChina Exploration and Development Research Institute and PetroChina Coalbed Methane Company Limited for picking up the samples.

## References

- [1] C. Zou, Q. Zhao, D. Dong et al., "Geological characteristics, main challenges and future prospect of shale gas," *Journal of Natural Gas Geoscience*, vol. 2, no. 5-6, pp. 273-288, 2017.

- [2] X. Guo, Y. Li, B. Tenger et al., "Hydrocarbon generation and storage mechanisms of deep-water shelf shales of Ordovician Wufeng Formation-Silurian Longmaxi Formation in Sichuan Basin," *Petroleum Exploration and Development*, vol. 47, no. 1, pp. 193–201, 2020.
- [3] Z. Jiang, Y. Song, X. Tang et al., "Controlling factors of marine shale gas differential enrichment in southern China," *Petroleum Exploration and Development*, vol. 47, no. 3, pp. 661–673, 2020.
- [4] C. Zou, D. Dong, Y. Wang et al., "Shale gas in China: characteristics, challenges and prospects (I)," *Petroleum Exploration and Development*, vol. 42, no. 6, pp. 753–767, 2015.
- [5] Y. Li, J. Yang, Z. Pan, S. Meng, K. Wang, and X. Niu, "Unconventional natural gas accumulations in stacked deposits: a discussion of upper Paleozoic coal-bearing strata in the east margin of the Ordos Basin, China," *Acta Geologica Sinica*, vol. 93, no. 1, pp. 111–129, 2019.
- [6] J. Liu, K. Liu, and X. Huang, "Effect of sedimentary heterogeneities on hydrocarbon accumulations in the Permian Shanxi Formation, Ordos Basin, China: insight from an integrated stratigraphic forward and petroleum system modelling," *Marine and Petroleum Geology*, vol. 76, pp. 412–431, 2016.
- [7] W. Ding, D. Zhu, J. Cai, M. Gong, and F. Chen, "Analysis of the developmental characteristics and major regulating factors of fractures in marine-continental transitional shale-gas reservoirs: a case study of the Carboniferous-Permian strata in the southeastern Ordos Basin, central China," *Marine and Petroleum Geology*, vol. 45, pp. 121–133, 2013.
- [8] Y. Li, Z. Wang, Z. Pan, X. Niu, Y. Yu, and S. Meng, "Pore structure and its fractal dimensions of transitional shale: a cross-section from east margin of the Ordos Basin, China," *Fuel*, vol. 241, pp. 417–431, 2019.
- [9] L. Kuang, D. Dong, W. He et al., "Geological characteristics and development potential of transitional shale gas in the east margin of the Ordos Basin, NW China," *Petroleum Exploration and Development*, vol. 47, no. 3, pp. 471–482, 2020.
- [10] W. Dang, J. Zhang, X. Tang et al., "Shale gas potential of Lower Permian marine-continental transitional black shales in the southern North China Basin, Central China: characterization of organic geochemistry," *Journal of Natural Gas Science and Engineering*, vol. 28, pp. 639–650, 2016.
- [11] M. M. Labani, R. Rezaee, A. Saeedi, and A. A. Hinai, "Evaluation of pore size spectrum of gas shale reservoirs using low pressure nitrogen adsorption, gas expansion and mercury porosimetry: a case study from the Perth and Canning Basins, Western Australia," *Journal of Petroleum Science and Engineering*, vol. 112, pp. 7–16, 2013.
- [12] Y. Li, D. Tang, P. Wu et al., "Continuous unconventional natural gas accumulations of Carboniferous-Permian coal-bearing strata in the Linxing area, northeastern Ordos basin, China," *Journal of Natural Gas Science and Engineering*, vol. 36, pp. 314–327, 2016.
- [13] IUPAC (International Union of Pure and Applied Chemistry), "Physical chemistry division commission on colloid and surface chemistry, subcommittee on characterization of porous solids: recommendations for the characterization of porous solids (technical report)," *Pure and Applied Chemistry*, vol. 66, no. 8, pp. 1739–1797, 1994.
- [14] D. J. K. Ross and R. M. Bustin, "The importance of shale composition and pore structure upon gas storage potential of shale gas reservoirs," *Marine and Petroleum Geology*, vol. 26, no. 6, pp. 916–927, 2009.
- [15] R. G. Loucks, R. M. Reed, S. C. Ruppel, and D. M. Jarvie, "Morphology, genesis, and distribution of nanometer-scale pores in siliceous mudstones of the Mississippian Barnett shale," *Journal of Sedimentary Research*, vol. 79, no. 12, pp. 848–861, 2009.
- [16] G. R. L. Chalmers and R. M. Bustin, "The organic matter distribution and methane capacity of the Lower Cretaceous strata of Northeastern British Columbia, Canada," *International Journal of Coal Geology*, vol. 70, no. 1–3, pp. 223–239, 2007.
- [17] G. R. L. Chalmers and R. M. Bustin, "Lower cretaceous gas shales in northeastern British Columbia, part I: geological controls on methane sorption capacity," *Bulletin of Canadian Petroleum Geology*, vol. 56, no. 1, pp. 1–21, 2008.
- [18] T. Cao, Z. Song, S. Wang, X. Cao, Y. Li, and J. Xia, "Characterizing the pore structure in the Silurian and Permian shales of the Sichuan basin, China," *Marine and Petroleum Geology*, vol. 61, pp. 140–150, 2015.
- [19] F. Gao, Y. Song, Z. Li et al., "Lithofacies and reservoir characteristics of the Lower Cretaceous continental Shahezi Shale in the Changling Fault Depression of Songliao Basin, NE China," *Marine and Petroleum Geology*, vol. 98, pp. 401–421, 2018.
- [20] S. Guo and W. Mao, "Division of diagenesis and pore evolution of a Permian Shanxi shale in the Ordos Basin, China," *Journal of Petroleum Science and Engineering*, vol. 182, article 106351, 2019.
- [21] H. Hu, F. Hao, X. Guo, F. Dai, Y. Lu, and Y. Ma, "Investigation of methane sorption of overmature Wufeng-Longmaxi shale in the Jiaoshiba area, Eastern Sichuan Basin, China," *Marine and Petroleum Geology*, vol. 91, pp. 251–261, 2018.
- [22] C. Lei, Z. Jiang, K. Liu, J. Tian, F. Gao, and P. Wang, "Pore structure characterization for organic-rich lower Silurian shale in the Upper Yangtze Platform, South China: a possible mechanism for pore development," *Journal of Natural Gas Science and Engineering*, vol. 46, pp. 1–15, 2017.
- [23] F. Wang, J. Guan, W. Feng, and L. Bao, "Evolution of overmature marine shale porosity and implication to the free gas volume," *Petroleum Exploration and Development*, vol. 40, no. 6, pp. 819–824, 2013.
- [24] M. Wang, R. W. T. Wilkins, G. Song et al., "Geochemical and geological characteristics of the Es<sub>3</sub><sup>L</sup> lacustrine shale in the Bonan sag, Bohai Bay Basin, China," *International Journal of Coal Geology*, vol. 138, pp. 16–29, 2015.
- [25] G. R. Chalmers, R. M. Bustin, and I. M. Power, "Characterization of gas shale pore systems by porosimetry, pycnometry, surface area, and field emission scanning electron microscopy/transmission electron microscopy image analyses: examples from the Barnett, Woodford, Haynesville, Marcellus, and doing units," *AAPG Bulletin*, vol. 96, no. 6, pp. 1099–1119, 2012.
- [26] L. Wang, S. Wang, R. Zhang et al., "Review of multi-scale and multi-physical simulation technologies for shale and tight gas reservoirs," *Journal of Natural Gas Science and Engineering*, vol. 37, pp. 560–578, 2017.
- [27] Y. Li, J. Chen, D. Elsworth, Z. Pan, and X. Ma, "Nanoscale mechanical property variations concerning mineral composition and contact of marine shale," *Geoscience Frontiers*, vol. 13, no. 4, article 101405, 2022.
- [28] T. Zhang, G. Ellis, S. Ruppel, K. Milliken, and R. Yang, "Effect of organic-matter type and thermal maturity on methane adsorption in shale-gas systems," *Organic Geochemistry*, vol. 47, pp. 120–131, 2012.

- [29] M. Wang, H. Xue, S. Tian, R. W. T. Wilkins, and Z. Wang, "Fractal characteristics of upper cretaceous lacustrine shale from the Songliao basin, NE China," *Marine and Petroleum Geology*, vol. 67, pp. 144–153, 2015.
- [30] Y. Li, J. Yang, Z. Pan, and W. Tong, "Nanoscale pore structure and mechanical property analysis of coal: an insight combining AFM and SEM images," *Fuel*, vol. 260, article 116352, 2020.
- [31] R. Yang, S. He, J. Yi, and Q. Hu, "Nano-scale pore structure and fractal dimension of organic-rich Wufeng-Longmaxi shale from Jiaoshiba area, Sichuan Basin: investigations using FE-SEM, gas adsorption and helium pycnometry," *Marine and Petroleum Geology*, vol. 70, pp. 27–45, 2016.
- [32] Z. Li, D. Liu, Y. Cai, Y. Wang, and J. Teng, "Adsorption pore structure and its fractal characteristics of coals by N<sub>2</sub> adsorption/desorption and FESEM image analyses," *Fuel*, vol. 257, article 116031, 2019.
- [33] H. Deng, X. Hu, H. A. Li, B. Luo, and W. Wang, "Improved pore-structure characterization in shale formations with FESEM technique," *Journal of Natural Gas Science and Engineering*, vol. 35, pp. 309–319, 2016.
- [34] S. Zhao, Y. Li, Y. Wang, Z. Ma, and X. Huang, "Quantitative study on coal and shale pore structure and surface roughness based on atomic force microscopy and image processing," *Fuel*, vol. 244, pp. 78–90, 2019.
- [35] J. Cui, D. Liu, Y. Cai, Z. Pan, and Y. Zhou, "Insights into fractures and minerals in subbituminous and bituminous coals by FESEM-EDS and X-ray  $\mu$ -CT," *Fuel*, vol. 237, pp. 977–988, 2019.
- [36] A. Li, W. Ding, J. He, P. Dai, S. Yin, and F. Xie, "Investigation of pore structure and fractal characteristics of organic-rich shale reservoirs: a case study of Lower Cambrian Qiongzhusi Formation in Malong block of eastern Yunnan Province, South China," *Marine and Petroleum Geology*, vol. 70, pp. 46–57, 2016.
- [37] H. Tian, S. C. Zhang, S. B. Liu, and H. Zhang, "Determination of organic-rich shale pore features by mercury injection and gas adsorption methods," *Acta Petrolia Sinica*, vol. 33, no. 3, pp. 419–427, 2012.
- [38] G. Sang, S. Liu, R. Zhang, D. Elsworth, and L. He, "Nanopore characterization of mine roof shales by SANS, nitrogen adsorption, and mercury intrusion: impact on water adsorption/retention behavior," *International Journal of Coal Geology*, vol. 200, pp. 173–185, 2018.
- [39] Y. Yao and D. Liu, "Comparison of low-field NMR and mercury intrusion porosimetry in characterizing pore size distributions of coals," *Fuel*, vol. 95, pp. 152–158, 2012.
- [40] C. R. Clarkson, M. Freeman, L. He et al., "Characterization of tight gas reservoir pore structure using USANS/SANS and gas adsorption analysis," *Fuel*, vol. 95, pp. 371–385, 2012.
- [41] C. R. Clarkson, N. Solano, R. M. Bustin et al., "Pore structure characterization of North American shale gas reservoirs using USANS/SANS, gas adsorption, and mercury intrusion," *Fuel*, vol. 103, pp. 606–616, 2013.
- [42] Y. Wang, Y. Zhu, S. Liu, and R. Zhang, "Pore characterization and its impact on methane adsorption capacity for organic-rich marine shales," *Fuel*, vol. 181, pp. 227–237, 2016.
- [43] F. Lai, Z. Li, W. Zhang, H. Dong, F. Kong, and Z. Jiang, "Investigation of pore characteristics and irreducible water saturation of tight reservoir using experimental and theoretical methods," *Energy & Fuels*, vol. 32, no. 3, pp. 3368–3379, 2018.
- [44] S. Guo and Y. Wang, "Shale gas accumulation conditions and exploration potential of carboniferous Benxi Formation in Ordos Basin," *Acta Petrolia Sinica*, vol. 34, pp. 445–452, 2013.
- [45] J. Schoenherr, R. Littke, J. L. Urai, P. Kukla, and Z. Rawahi, "Polyphase thermal evolution in the Infra-Cambrian Ara Group (South Oman Salt Basin) as deduced by maturity of solid reservoir bitumen," *Organic Geochemistry*, vol. 38, no. 8, pp. 1293–1318, 2007.
- [46] J. Teng, H. Deng, B. Liu et al., "Insights of the pore system of lacustrine shales from immature to late mature with the aid of petrology, mineralogy and porosimetry: a case study of the Triassic Yanchang Formation of the Ordos Basin, North China," *Journal of Petroleum Science and Engineering*, vol. 196, article 107631, 2021.
- [47] E. W. Washburn, "Note on a method of determining the distribution of pore sizes in a porous material," *Proceedings of the National Academy of Sciences of the United States of America*, vol. 7, no. 4, pp. 115–116, 1921.
- [48] K. S. W. Sing, D. H. Everett, and R. A. W. Haul, "Reporting physisorption data for gas/solid systems with special reference to the determination of surface area and porosity," *Pure and Applied Chemistry*, vol. 57, no. 4, pp. 603–619, 1985.
- [49] Z. Xi, S. Tang, J. Wang, G. Yang, and L. Li, "Formation and development of pore structure in marine-continental transitional shale from northern China across a maturation gradient: insights from gas adsorption and mercury intrusion," *International Journal of Coal Geology*, vol. 200, pp. 87–102, 2018.
- [50] X. Yang, Z. Jiang, Y. Song et al., "A comparative study on whole-aperture pore structure characteristics between niutitang and longmaxi formation of high-maturity marine shale in southeastern Chongqing," *Geological Journal of China Universities*, vol. 22, no. 2, pp. 368–377, 2016.
- [51] Z. Jiang, X. Tang, Z. Li et al., "The whole-aperture pore structure characteristics and its effect on gas content of the Longmaxi Formation shale in the Sichuan basin," *Earth Science Frontiers*, vol. 23, pp. 127–134, 2016.
- [52] H. Hu, F. Hao, J. Lin, Y. Lu, Y. Ma, and Q. Li, "Organic matter-hosted pore system in the Wufeng-Longmaxi (O<sub>3</sub>w-S<sub>1</sub>1) shale, Jiaoshiba area, Eastern Sichuan Basin, China," *International Journal of Coal Geology*, vol. 173, pp. 40–50, 2017.
- [53] Y. Li, X. Li, Y. Wang, and Q. Yu, "Effects of composition and pore structure on the reservoir gas capacity of Carboniferous shale from Qaidam Basin, China," *Marine and Petroleum Geology*, vol. 62, pp. 44–57, 2015.
- [54] Y. Sun and S. Guo, "Characterization of whole-aperture pore structure and its effect on methane adsorption capacity for transitional shales," *Energy & Fuels*, vol. 32, no. 3, pp. 3176–3188, 2018.
- [55] K. Zhao and S. Guo, "Characteristics and main controlling factors of shale gas reservoirs in transitional facie: a case study of Upper Paleozoic in Ordos Basin," *Petroleum Exploration and Development*, vol. 37, no. 2, pp. 141–149, 2015.
- [56] Y. Zhu, Y. Wang, S. Cheng, H. Zhang, and C. Fu, "Qualitative-quantitative multiscale characterization of pore structures in shale reservoirs: a case study of Longmaxi Formation in the upper Yangtze area," *Earth Science Frontiers*, vol. 23, pp. 154–163, 2016.
- [57] S. Shi, Y. Wang, H. Guo, C. Chen, and R. Deng, "Variations in pore structure of marine shale from the same horizon of the Longmaxi Formation with changing position in a small-scale anticline: implications for the influence of structural

- deformation,” *Marine and Petroleum Geology*, vol. 124, article 104837, 2021.
- [58] J. Yan, S. Zhang, J. Wang, Q. Hu, M. Wang, and J. Chao, “Applying fractal theory to characterize the pore structure of lacustrine shale from the Zhanhua Depression in Bohai Bay Basin, Eastern China,” *Energy & Fuels*, vol. 32, no. 7, pp. 7539–7556, 2018.
- [59] W. Sun, Y. J. Zuo, Z. H. Wu et al., “Pore characteristics and evolution mechanism of shale in a complex tectonic area: case study of the Lower Cambrian Niutitang Formation in Northern Guizhou, Southwest China,” *Journal of Petroleum Science and Engineering*, vol. 193, article 107373, 2020.
- [60] Q. R. Passey, K. M. Bohacs, and W. L. Esch, “From oil-prone source rock to gas-producing shale reservoir-geologic and petrophysical characterization of unconventional shale gas reservoirs,” in *CPS/SPE International Oil & Gas Conference and Exhibition in China*, Beijing, 2010 Society of Petroleum Engineers.
- [61] J. Zhong, G. Chen, C. Lv et al., “Experimental study of the impact on methane adsorption capacity of continental shales with thermal evolution,” *Journal of Natural Gas Geoscience*, vol. 1, no. 2, pp. 165–172, 2016.
- [62] T. Lin, W. Duan, H. Ren, and X. Lu, “The formation and evolution of shale pore space and pore effects to gas bearing capacity,” *China Journal Geology*, vol. 52, no. 1, pp. 141–155, 2017.